

## Investigation of Single-step Fabrication of a Cathode-supported Planar Single-chamber Solid Oxide Fuel Cell and Its Performance

Yunus SAYAN<sup>1,2\*</sup>, Jung-Sik KİM<sup>2</sup>, Houzheng WU<sup>2</sup>

<sup>1</sup> Bitlis Eren University, Faculty of Engineering and Architecture, Department of Mechanical Engineering, Bitlis, Türkiye

<sup>2</sup> Loughborough University, School of Aeronautical, Automotive, Chemical and Material Engineering Loughborough, United Kingdom

(ORCID: [0000-0002-0871-6842](https://orcid.org/0000-0002-0871-6842)) (ORCID: [0000-0002-3696-7251](https://orcid.org/0000-0002-3696-7251)) (ORCID: [0000-0002-7628-3890](https://orcid.org/0000-0002-7628-3890))



**Keywords:** Solid oxide fuel cell (SOFC); Co-sintering; Cell manufacturing; Cell performance; Cell microstructure.

### Abstract

This study presents a cathode-supported planar solid oxide fuel cell (SOFC) fabrication made via a single step co-sintering method and investigation of its performance. The materials used are NiO-CGO, CGO and CGO-LSCF for anode, cathode, electrolyte, respectively. Our study shows that increasing the cell size has a detrimental effect on cell single step co-sinterability. Increasing cathode thickness and reducing electrolyte thickness led to curvature decrease at the edges, however these adjustments were not enough to achieve a curvature-free cathode-supported cell. Thus, three porous alumina cover plates (total mass of 49.35 g) placed on the top of the cell during sintering were utilized to suppress curvature formation, and as a result, a nearly curvature-free cathode-supported cell was obtained. Performance of the cells were investigated. The results showed that increasing cathode thickness and decreasing electrolyte thickness had negative effects on cell performance despite enhanced single step co-sinterability of the cell. The maximum power density and OCV of the final planar cell (thickness 60-40-800  $\mu\text{m}$ , anode-electrolyte-cathode) were found to be 1.71  $\text{mW cm}^{-2}$  and 0.2 V, respectively, in a fuel rich condition (R:1.6). Additionally, the maximum OCV and power density among the all cells were measured from the cell (thickness 60-40-400  $\mu\text{m}$ , anode-electrolyte-cathode) as 0.56 V and 24.79  $\text{mW cm}^{-2}$ , respectively, in a fuel rich condition (R:2.4).

## 1. Introduction

A new type of solid oxide fuel cell (SOFC), single chamber solid oxide fuel cells (SC-SOFCs), were introduced by researchers to reduce certain drawbacks faced in dual chamber SOFCs (DC-SOFCs), such as complex gas manifolding, flow field structures and gas-tight sealing [1]. Unlike DC-SOFCs, SC-SOFCs are composed of only one gas chamber containing a gas mixture of fuel and oxidant [1]–[4]. This distinctive characteristic of SC-SOFCs allows them to have simplified structures, resulting in less start-up and shut down time and better thermal shock resistance than DC-SOFCs [1], [3], [5]. If their

potential is released, the simplified structure could yield a considerable decrease of the total system cost. Moreover, the electrolyte layer does not have to be dense to stop gas crossover, given that there is no requirement prevent fuel mixing with oxidant gas. This property of SC-SOFCs enables utilization of less expensive manufacturing methods of the electrolyte.

For the anode supported SOFCs, potential anode re-oxidation is a serious problem which can cause cells to break after repeated cycles of cell usage [6], [7]. This is because the thicker anode (based on nickel, Ni) catalyst oxidation and reduction lead to cell to shrink and expand in time. This uncontrolled

\* Corresponding author: [ysayan@beu.edu.tr](mailto:ysayan@beu.edu.tr)

Received:31.10.2023, Accepted:15.01.2024

volume shrinkage and expansion leads the cell to crack. Therefore, a new configuration of SOFCs, named as cathode-supported SOFC, were proposed by researchers to overcome this issue [1], [3]. This configuration of SOFC has showed the longest lifetime among all categories of SOFCs [8], but incurs penalties on the sluggish oxygen reduction reaction overpotentials.

Using co-sintering process for multi-layer structures leads to considerable benefits in time, energy savings and effort, and thus has been attracting growing interest in many different research areas, including SOFCs. In the production of DC-SOFCs, co-sintering has been generally applied to bi-layer structures, comprising of anode and electrolyte layers. It is because the similar sintering behavior of each layer inhibits developments of any defects such as warping, delamination and cracking during the sintering process [9]–[11].

SC-SOFCs are currently fabricated utilizing at least two sintering process: usually co-sintering anode and electrolyte, followed by a separate deposition of the cathode and its sintering [12]–[14]. The prevailing explanation for a two-step sintering is that the materials for electrolyte, cathode and anode need different sintering temperatures to obtain the required microstructures. Though possible reactions/interactions between electrolyte and cathode are reduced by a two-step sintering process [14], there are some rationales why single-step co-sintering (SSCS) of SC-SOFCs, sintering anode, cathode and electrolyte together in one step, are desired. It is primarily needed to simplify the fabrication process along with lessening the processing time and input energy [15], [16]. These advantages of single step co-sintering of SC-SOFCs decrease further the fabrication cost of SC-SOFCs and thus improve commercial viability if used in commercial scale. However, when multiple layers are sintered together, they impose stress upon each other due to the different shrinkage behavior, and thereby resulting in either curvature formation, delamination or cracks in the cell.

In this study, the SSCS of cathode-supported SC-SOFCs was investigated profoundly. The effect of layer thickness, cell size and sintering temperature on cell sinterability were analyzed. In order to achieve a curvature free cathode-supported cell, a limiting constraint was applied on the top of the cells. The fabricated cells were then tested under single chamber conditions so as to observe the functionality of the cells as working electrochemical cells and to analyze the effect of thickness and thickness ratio change on the cell performance.

## 2. Experimental

### 2.1. Preparation of the Cells

Cell green layers were procured from Maryland tape casting Ltd, USA [17]. They were all made by tape casting method, consisting of 60 wt% NiO (nickel oxide)–40 wt%  $\text{Ce}_{0.8}\text{Gd}_{0.2}\text{O}_{2-\delta}$  (gadolinium doped ceria (CGO)):  $\text{Ce}_{0.8}\text{Gd}_{0.2}\text{O}_{2-\delta}$  (CGO): 50 wt%  $\text{La}_{0.6}\text{Sr}_{0.4}\text{Co}_{0.2}\text{Fe}_{0.8}\text{O}_{3-\delta}$  (lanthanum strontium cobalt ferrite (LSCF))–50 wt% CGO (20% gadolinium(Gd)) as anode-electrolyte-cathode, (A-E-C). The slurry composition of the green tapes provided by the supplier are summarized in reference [18]. The sintering temperature of the LSCF cathode is less than that of the anode and electrolyte [19], [20]. Therefore, in order to retard the sintering behavior of the LSCF and thereby balancing the final density of materials during the process of co-sintering, the LSCF particle size was chosen to be larger than that of the anode and cathode (1  $\mu\text{m}$  for the cathode green tape as opposed to 0.3  $\mu\text{m}$  for the anode and electrolyte green tapes).

Multiple layers of green tapes were layered upon each other to obtain desired thickness of electrolyte and electrodes. Each component thickness was controlled by the number of individual green tape layers of each material (of around 20  $\mu\text{m}$  for each tape). These layers are subsequently hot-pressed at a pressure of 2 MPa and temperature 60 °C dwelling for 5 minutes (using the Carvel Heated Bench Top Hot Press, model: 3853CE-8, USA) to allow individual layers to merge and form a complete cell. The hot pressing condition was carefully determined in order to achieve acceptable compactness and good adhesion between each layer, and also prevent over-pressing and inhomogeneous cell area distribution (detailed explanation is available in ref. [18]).

Thickness of each layer in a cell can have direct effect on as-sintered cell quality through co-sintering. In order to investigate such influence, several cells with different combinations of thicknesses were prepared. All cells were hot pressed under same conditions. Subsequently sintered at 1200 °C with a 1 hour of dwelling time under a heating and cooling rate profile as following: a 1 °C  $\text{min}^{-1}$  heating rate from room temperature to 500 °C, 2 °C  $\text{min}^{-1}$  from 500 °C to 900 °C, 1 °C  $\text{min}^{-1}$  from 900 °C to 1200 °C; and a 3 °C  $\text{min}^{-1}$  cooling rate from 1200 °C to room temperature. Sintering profile of the cells were thoroughly defined with the purpose of achieving less defects during single-step co-sintering fabrication processes by carefully analyzing debinding and shrinkage properties of each green

layer (detailed information is presented in reference [18]).

In order to investigate the effect of sintering behavior of a cathode-supported cell during heating and during cooling, a cell with a thickness ratio and thickness of 3-2-10 and 60-40-200  $\mu\text{m}$ , respectively, were made (anode-electrolyte-cathode), with a 40x40 mm width (W) and length (L). In addition, two types of cells with different cathode thicknesses were made with the aim of investigating the cathode thickness and the cell size on cell SSCS. The first type of cell possessed a width and length of 40 mm and 40 mm (named cell type 1) respectively while the second type had a 30x30 mm W x L (named cell type 2). For both type of cells, cathode thickness increased from 200  $\mu\text{m}$ , to 300  $\mu\text{m}$ , and to 400  $\mu\text{m}$  while anode and

electrolyte thickness were kept constant with a thickness of 60  $\mu\text{m}$  and 40  $\mu\text{m}$ , respectively. Moreover, three different types of the cells were prepared to investigate the effect of electrolyte thickness and limited constraint on single step co-sinterability. They are named as cell 1, cell 2 and cell 3, having the same width and length (40x40 mm WxL), as listed in Table 1. Cell 3 was initially sintered without any constraint, but later iterations were sintered with either one or multiple alumina ( $\text{Al}_2\text{O}_3$ ) porous cover plates (1 mm thickness, 40% porosity, ESLTM 42520-2) located on the top of the cell. This improved the ability to restrain curvature formation, and finally to achieve a curvature-free cell.

**Table 1.** Three different cathode-supported SC-SOFCs, their thicknesses, thickness ratio, and sintering type.

Cell Type	Thickness Ratio anode:electrolyte:cathode	Thickness / $\mu\text{m}$ anode:electrolyte:cathode	Sintering Type
Cell 1	3-2-20	60-40-400	Without any constraint on the top layer of the cell
Cell 2	3-1-20	60-20-400	Without any constraint on the top layer of the cell
Cell 3	3-1-40	60-20-800	Without any constraint on the top layer of the cell
Cell 3	3-1-40	60-20-800	Sintered with a 50x50 mm LxW porous alumina cover plate on the top of the cell, with a total mass of 7.31 g
Cell 3	3-1-40	60-20-800	Sintered with a 75x75 mm LxW porous alumina cover plate on the top of the cell, with a total mass of 16.45 g
Cell 3	3-1-40	60-20-800	Sintered with two 75x75 mm LxW porous alumina cover plates on the top of the cell, with a total mass of 32.9 g
Cell 3	3-1-40	60-20-800	Sintered with three 75x75 mm LxW porous alumina cover plates on the top of the cell, with a total mass of 49.35 g

## 2.2. Characterizations and Tests

In order to characterize the microstructure of as-sintered cell as well as chemical element of the final planar cell, scanning electron microscopy (SEM) with energy dispersive spectroscopy (EDS) (Zeiss 1530-VP FEGSEM, Germany) was used. Acceleration voltage for imaging by backscattered electrons and secondary electrons was set to 20 kV and 5 kV, respectively. A layer of palladium-gold (Pd-Au) alloy was sputtered all examined surfaces to prevent charging during imaging. All EDS spectra were obtained as an acceleration voltage of 20 kV. Grinding and polishing were carefully applied to the final cell in order to accurately examine the grain size and pore structure of an as-sintered cell by using

semi-automatic Struers LaboSystem (Germany), after the cell was mounted in Bakelite by using Struers CitoPress 5 (Germany).

The porosity of the cell was quantified by applying the ImageJ program to the obtained SEM images. The method used to estimate the mean porosity of the cathode, electrolyte and anode of the cell and can be detailed as follows: Back scatter SEM images of the anode, cathode and electrolyte cross-sectional areas of the cell were taken separately. All images possess a 10  $\mu\text{m}$  scale, Mag 2.00 KX, and WD of 8.5 mm. Thereafter, obtained images were uploaded to ImageJ program and were set to 8-bit image quality for threshold analysis. Adjustment for the threshold of each images was carefully done. The percentage of the pore area were read and recorded

by measuring the percentage of black area on the images.

A potentiostat (Solartron Analytical 1280C, United Kingdom) in concert with the CorrWare®/CorrView™ electrochemical suite (Scribner Associates Inc., United States) was used to measure the open circuit voltage (OCV) and polarization of the cells. In addition, Q150T S/E/ES Turbo-Pumped Sputter Coater (Quorum Technologies, United Kingdom) was utilized to sputter gold on both electrodes as current collector. Silver paste was used to attach chromel (90% Ni, 10% chromium (Cr)) wire to sputtered gold grids. A single chamber condition was applied in order to test cells. All cells were positioned in an alumina cell holder perpendicular to flow direction. Additionally, all anode electrodes of the cells were initially reduced at 600 °C for 1 hour in a flowing gas mixture of hydrogen and nitrogen with a flowing rate of 0.01 L min<sup>-1</sup>, and 0.19 L min<sup>-1</sup>, respectively. Following reduction, those cells were tested in a flowing mixture of gas with different compositions at 600 °C.

### 3. Results and Discussion

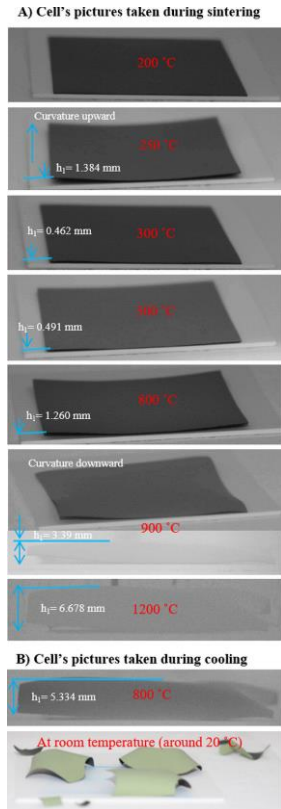
#### 3.1. Sintering Results

##### 3.1.1. Sintering Behavior of a Cathode-Supported Cell During Heating and During Cooling

Figure 1 depicts the picture of a cathode-supported cell taken during sintering and cooling at different temperatures (thickness ratio and thickness of the cell are 3-2-10 and 60-40-200 μm, respectively, (anode-electrolyte-cathode), with a 40x40 mm width and length. The cell was placed on a porous alumina substrate, with the cathode adjacent to it (facing downward). According to Figure 1A, there is no observable/substantial curvature formation up to 200 °C. However, when temperature reached 250 °C, there is a visible curvature formation towards the upward direction,  $h_1 = 1.384$  mm, (curvature height,  $h_1$ , from top surface of alumina substrate to the peak point of the top surface of the cell). This might be as a result of additives removal in the green body during debinding stage. Because the top surface of the cell is the drying surface and additives will be first evaporated from the top surface. This phenomenon leads to a capillary force in the top surface and cause a compressive stress in this area. Therefore, cells curved towards upward. Moreover, when the temperature reached to 300 °C, the cell curvature was relieved, the  $h_1$  decreased to 0.462 mm. This could be explained by the fact that later into the drying process

(above 250 °C and until the end of the additive removal process (500 °C)), the liquid vapor interface is subjected to changes from the top surface to the interior of the green body and pores are occupied with air. This results in a reduction in compressive stress on the top surface. In addition, the lower part of the green body still contains liquid therefore it is exposed to compressive stress due to capillary forces. This brings about the tendency of the green body to warp into the opposite direction. In general, the effect of capillary force, at the lower part of the cell at the later stage of sintering was not big enough to curve cell downward. Thus, the cell curvature was still upward after the burn-out stage. Additionally, the curvature direction is still upward until 800 °C, and the curvature height reached to 1.260 mm. It might be as a result of particle rearrangement. However, when the main densification started (after 800 °C), the cells edges tended to curve downward due to higher shrinkage rate of cathode which is the fact that high shrinkage of the cathode generates high compressive stress on the bottom of the cell and thus leads to more curvature formation of the cells towards the cathode side. The curvature height became 3.39 mm at 900 °C though the effect of additive removals on curvature formation was still at present (see Figure 1A). Moreover, in the main densification area, cell curvature directed downward, and it reached its maximum value of 6.678 mm at 1200 °C (see Figure 1A).

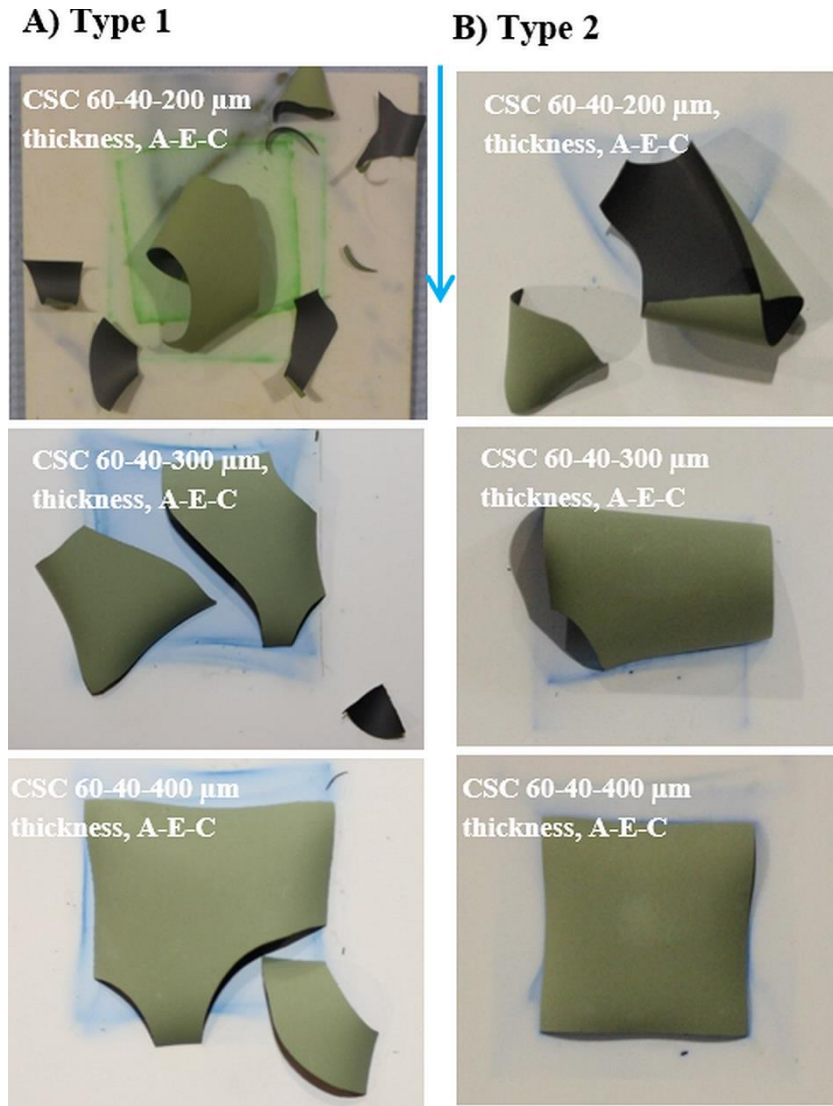
In addition, the main observation from these figures was that it was expected for the cell to crack when it reached at 1200 °C or after dwelling at 1200 °C. However, surprisingly, there was no cracking or delamination during heating and after dwelling as shown in Figure 1A. Nevertheless, when the cell was cooled down, the cell did not break until 800 °C. It might not even have broken at a temperature of less than 800 °C. However, the cell broke into many pieces during cooling owing to residual stress in the cell (see Figure 1B). It might be explained by the fact that, at elevated temperature, the ceramic cell might have possessed plastic properties and thus withstood high residual stress. However, when the temperature decreased, the cell became more brittle and the contribution of coefficient of thermal expansion (CTE) mismatch stress (due to three different layers of the cell) to sintering stress became higher at room temperature. Consequently, the cell could not withstand the amount of residual stress due to its brittle crystal structure.



**Figure 1.** The pictures of a cathode-supported cell taken A) during sintering and B) during cooling at different temperatures, thickness ratio and thickness of the cell are 3-2-10 and 60-40-200  $\mu\text{m}$ , respectively, (Anode-Electrolyte-Cathode), with a 40x40 mm width and length.

### 3.1.2. The Influence of Cathode Thickness and Cell Size On Cell SSCS

Figure 2 shows the sintering results of type 1 and type 2 cells. It can be clearly seen from the figure as a visual inspection for both type of cells, increasing cathode thickness improved cell SSCS. The following reasons are put forth: firstly, the cathode layer became more dominant in overall cell composition, thus, the individual effects of anode and cathode become less pronounced during sintering. Secondly, increased cathode thickness improved cell resistance to deformation and fracture, therefore, the cells become more robust towards withstanding either sintering stress during heating or CTE mismatch stress during cooling as a result of increased cross-sectional area of the cathode normal to the length direction. Furthermore, it can also be seen from the Figure 2, increasing cell size from 30x30 mm to 40x40 mm (WxL) has negative effect on SSCP. For instance, cell type 1 with a cathode thickness of 200  $\mu\text{m}$  broke into numerous pieces while cell type 2 for the same cathode thickness splintered into fewer pieces. Similarly, cell type 1 with a cathode thickness of 400  $\mu\text{m}$  broke into three parts whereas cell type 2 for the same cathode thickness has no cracks present after sintering.

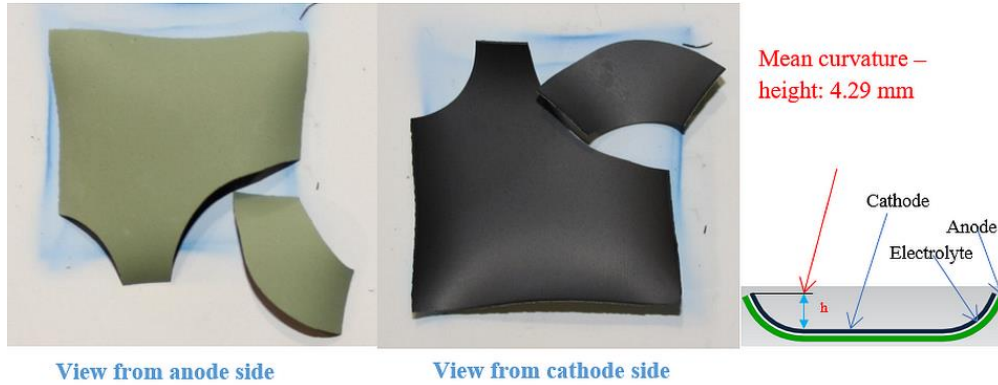
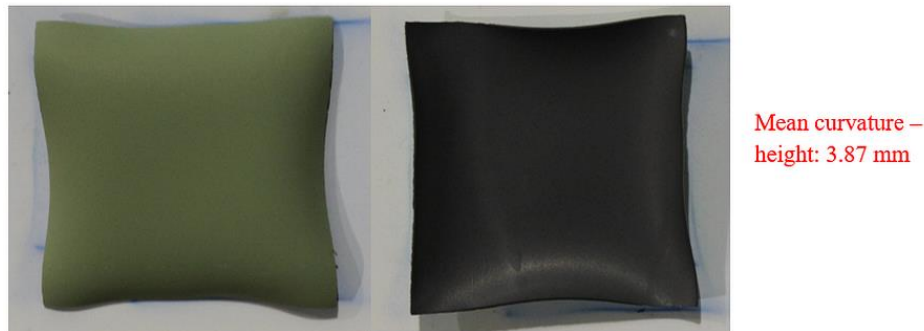


**Figure 2.** The influence of cathode thickness and cell size on cell sinterability, sintered at 1200 °C, A) Type 1: Cells` Width X Length 40x40 mm and B) Type 2: Cells` Width X Length 30x30 mm. CSC is the abbreviation of the cathode supported cell.

### 3.1.3. The Influence of Electrolyte Thickness On Cell SSCS

Figure 3 shows the sintering results of two different cathode-supported cells. Cell 1 and Cell 2 possess the same anode and cathode thickness (60 μm and 400 μm, respectively) while their electrolyte thickness is 40 μm and 20 μm, respectively. The figure shows that decreasing electrolyte thickness improved SSCS of

the cell. The cell mean curvature height decreased from 4.29 mm to 3.87 mm and there was no crack after sintering (see Figure 3, cell 1 and cell 2). This might be as a result of the electrolyte mismatch stress contribution mitigation. The mean curvature height,  $h$ , was calculated from the cathode top surface to the peak point of curves as shown in Figure 3. The measurement was carried out from each side of the cells and the average of them was taken.

**Cell 1 40 x 40 mm WxL thickness ratio 3-2-20 (A-E-C) thickness 60-40-400  $\mu\text{m}$** **Cell 2 40 x 40 mm WxL thickness ratio 3-1-20 (A-E-C) thickness 60-20-400  $\mu\text{m}$** 

**Figure 3.** The influence of electrolyte thickness on cell sinterability.

### 3.1.4. Constrained Sintering of Cathode-Supported Cells

For the cathode-supported cell, increasing cathode thickness continuously and decreasing electrolyte thickness was not enough to obtain curvature-free cells as seen in previous sections. In addition, concentration polarization becomes a serious problem when the cathode thickness is increased too much. This is because the thicker cathode causes impediments to the gas transport from top surface of the cathode to the inner pores of the cathode-electrolyte interface and product removal from triple phase boundary (TPB). This issue becomes more vital when a cell is placed as a flow-through (perpendicular to gas flow) arrangement in the mixture. Therefore, it is important to investigate different methods to remove curvature formation rather than continuously increasing cathode thickness. Placing a limiting constraint on the top of the cell was a useful approach to obtain curvature-free cells without changing the thickness of the cell as demonstrated in [18]. Therefore, five cells with the same size, thickness and thickness ratio were made and sintered either free or with limited constraint on the top of the cells. For that purpose, either one or

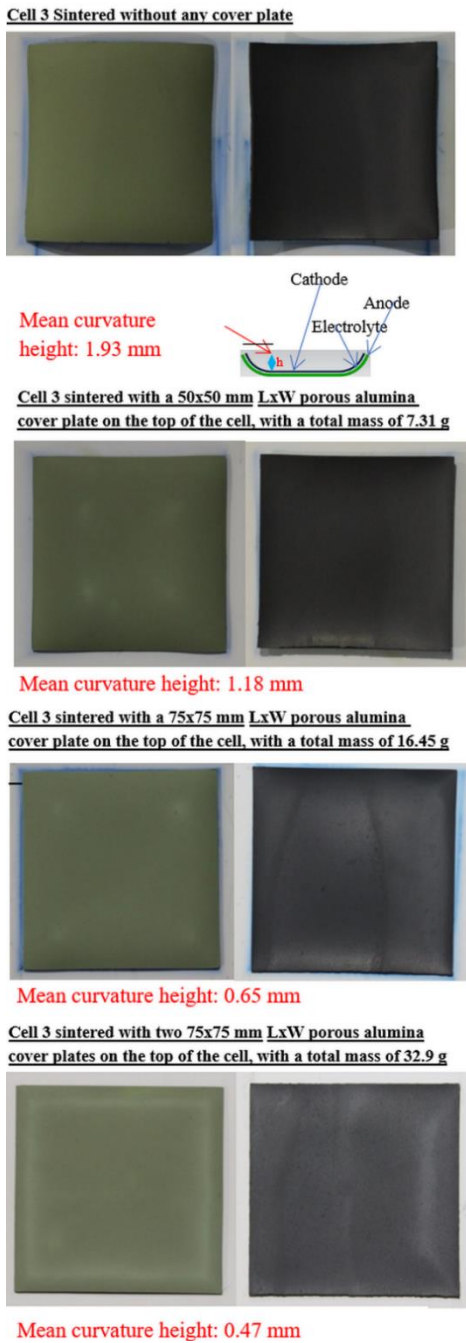
multiple alumina porous cover plates were located on the top of the cells during sintering so as to investigate the effect of the limited constraint on cell sinterability, the ability to suppress curvature formation, and finally to obtain curvature free cell. The cells were made with a 40x40 mm of WxL and a thickness of 60-20-800  $\mu\text{m}$  A-E-C (thickness ratio of 3-1-40). The porosity and thickness of alumina cover plate is around 40% and 1 mm, respectively. The length and width of the alumina cover plates can be seen in the Figure 4. The cells were sintered at 1200°C. Figure 4 depicts the sintering results of these cells.

According to Figure 4, the cell sintered with a 50x50 mm, WXL, porous alumina cover plate has less mean curvature height ( $h = 1.18$  mm) in comparison to the cell sintered without cover plate ( $h = 1.93$  mm). However, whilst sufficient for an anode supported cell, this mass of cover plate is not enough to suppress curvature evolution of the cathode-supported cell studied here. Furthermore, increasing cover plate mass (from 7.31 g to 16.45 g) by simply using a bigger size of porous cover plate (75x75 mm, WxL) reduced mean curvature height further (to 0.65 mm). Increasing porous cover plate mass has no linear effect on curvature reduction as can be seen

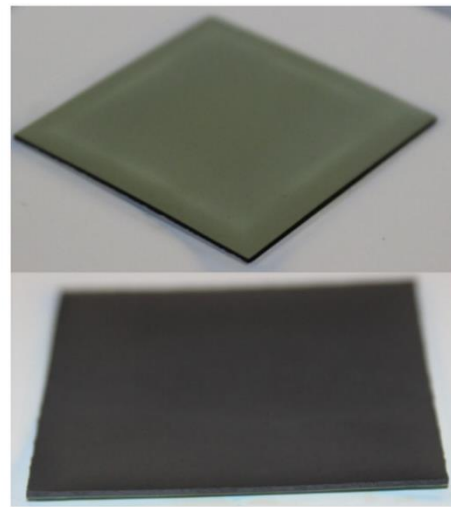
from Figure 4B. According to Figure 4B shows the relation of porous alumina cover plate mass with the mean curvature height with a possible equation,  $y = 0.391 + 1.539 \cdot \exp(-0.089 \cdot x)$ . It can be used to predict the mean curvature height with the change of the cover plate mass for the cathode-supported SC-SOFCs. Though the Figure 4B has limited data for its reliability, it can still give an approximate idea about required cover plate mass for curvature free cathode-supported cell for this type of cells with the same

size, thickness, and thickness ratio. Figure 4 shows the mean curvature height becomes almost stable after using two or more 75x75 mm cover plates on top of the cell (around 0.47 mm for two cover plate and 0.41 mm for three cover plates). To conclude, a cell with a low mean curvature height (0.41 mm) was obtained after using three 75x75 mm, WxL, alumina porous cover plates on the top of the cell during sintering.

**A) Free and limited constraint sintered of cathode supported cells**



Cell 3 sintered with three 75x75 mm LxW porous alumina cover plates on the top of the cell, with a total mass of 49.35 g



Mean curvature height: 0.41 mm

Estimated porosity:

Anode: % 24.31

Electrolyte: % 12.43

Cathode: % 26.04

**B) Estimated mean curvature height reduction with mass of the porous alumina cover plate and its possible equation**

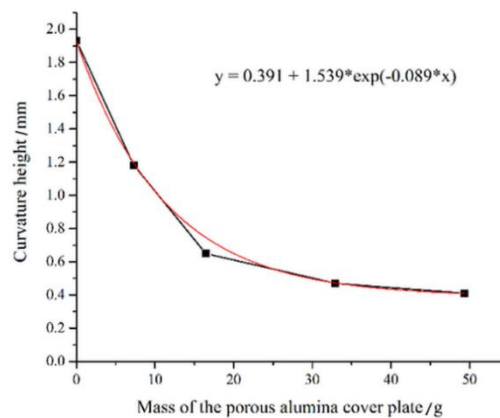


**Figure 4.** A) Free and limited constraint sintered of cathode-supported cells having the same width, length, thickness and thickness ratio (40mm, 40mm, 3-1-40 (A-E-C) and 60-20-800  $\mu\text{m}$  (A-E-C), respectively) and B) Estimated mean curvature height reduction with mass of the porous alumina cover plate used to suppress curvature formation and its possible equation.

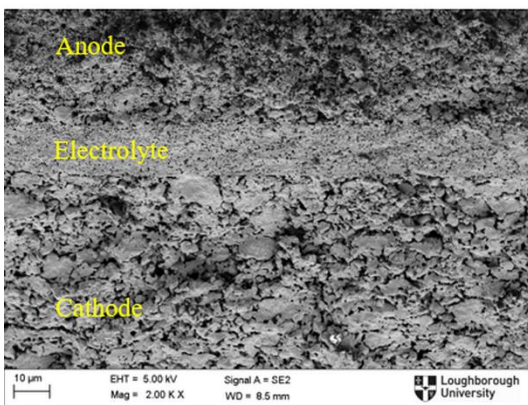
### 3.1.5. Characterization of Selected Optimum Specimen of Sintered Cells

Figure 5 displays the SE image of unpolished and BSE SEM images of polished nihai cell 3 sintered with three 75x75 mm LxW porous alumina cover plates on the top of the cell. When inspecting the SE and BSE SEM images in Figure 5, there is consistently good adhesion between anode-electrolyte, and cathode-electrolyte layers across the cell. However, it has a porous electrolyte (acceptable in the SC-SOFC configuration, but needs full densification for use in conventional DC-SOFCs). Moreover, in general for the cell, there is a good connection of NiO phase on anode side and LSCF phase on cathode side. However, the CGO continuity on both sides is not as good as desired. In addition, there is normal grain growth in all section of the cells;

however, the cathode in the cell possesses coarser microstructure than the anode as a consequence of over-sintering. Furthermore, from Figure 5, the estimated porosity of the anode, electrolyte and cathode for cell 3 was measured (by using ImageJ program) to be 24.11%, 12.43% and 26.04%, respectively (see Figure 4). In addition, for the same cell, the mean particle and pore size was found to be  $2.895 \pm 1.864 \mu\text{m}$  and  $1.267 \pm 0.723 \mu\text{m}$  for anode, respectively, and that of  $3.645 \pm 2.27 \mu\text{m}$  and  $1.603 \pm 0.736 \mu\text{m}$ , respectively, for cathode. It can be generally seen that cathode has higher porosity and mean pore size compared to that of the anode. This might be as a result of coarser microstructure of cathode because the increase in mean grain size is accompanied by a rise in the mean pore size.

#### CSC 3 sintered with three 75x75 mm LxW porous alumina cover plates on the top of the cell

A) Secondary electron (SE) SEM without polishing



B) Backscatter electron (BSE) SEM image, polished

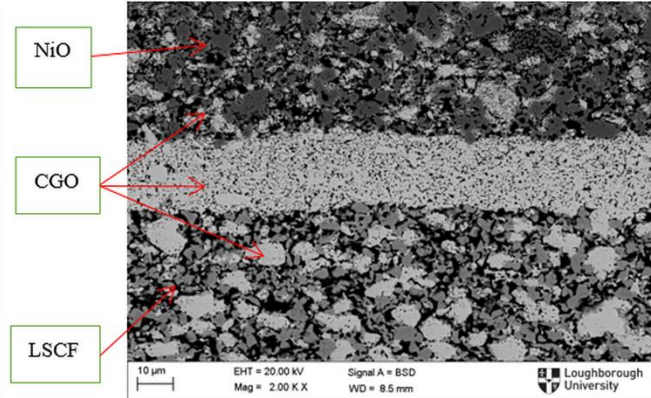


**Figure 5.** A) Unpolished SE SEM image of Cell 3 and BSE image of polished Cell 3, having the 40x40 mm WxL thickness ratio 3-1-40 (A-E-C), thickness 60-20-800  $\mu\text{m}$  sintered with three 75x75 mm LxW porous alumina cover plates on the top of the cell.

Figure 6 depicts the EDS spectrum of cell 3 (the final obtained cell) from anode and cathode side, respectively. The purpose taking of EDS analysis of cell 3 is to investigate possible impurities introduced during fabrications process. The EDS spectra of the cell shows all elements in the scanned region. Figure 6A shows the map sum spectrum of cell from the anode side. It can be observed that there is a small amount of gold, palladium, aluminum (Al), zirconium (Zr), silisyum or silicon (Si), strontium (Sr) and cobalt (Co). The existence of Au and Pd is due to the sputtering of these elements before SEM imaging in order to make the cell conductive. Aluminum might have been introduced during sintering either from alumina substrate or porous cover plate. Zirconium might have been introduced during ball milling by ball milling medium which is

made of yttria stabilized zirconia (YSZ). However, the existence of strontium and cobalt was due to the diffusion of these elements from cathode sides. Furthermore, silicon might be coming from different stages of the fabrication process since Si elements could be present in any of these stages. In addition, from the cathode side EDS spectrum (Figure 6B), there were also Au, Pd, Al, Zr, and Si elements on the cathode side due to the same respectively reasons mentioned for EDS spectrum analysis from the anode side. In addition to these contaminations, Ni was also detected on cathode side because of the nickel diffusion from the anode side. To conclude there were same contaminations on both sides of electrodes, and small amounts of anode- and cathode-side elements diffused from anode to cathode and cathode to anode, respectively. It is important to

avoid or to minimize this contamination to a reasonable level so as to obtain better performance from the cells, with regards to catalytic selectivity and favorable reactant concentration gradients at the respective electrodes.

Furthermore, Figure 6C displays X-Ray diffraction (XRD) patterns of the cell 3. According to this figure, there is no undesired phase formation

after sintering except the required phases (NiO, CGO and LSCF) for the cell. Though there were some impurities detected from EDS analysis in the previous paragraph, their reaction with other elements which form new phases such as silisium oxide (SiO), zirconium oxide (ZrO), cobalt oxide (CoO) and so forth were not observed in XRD patterns due to their small amount.

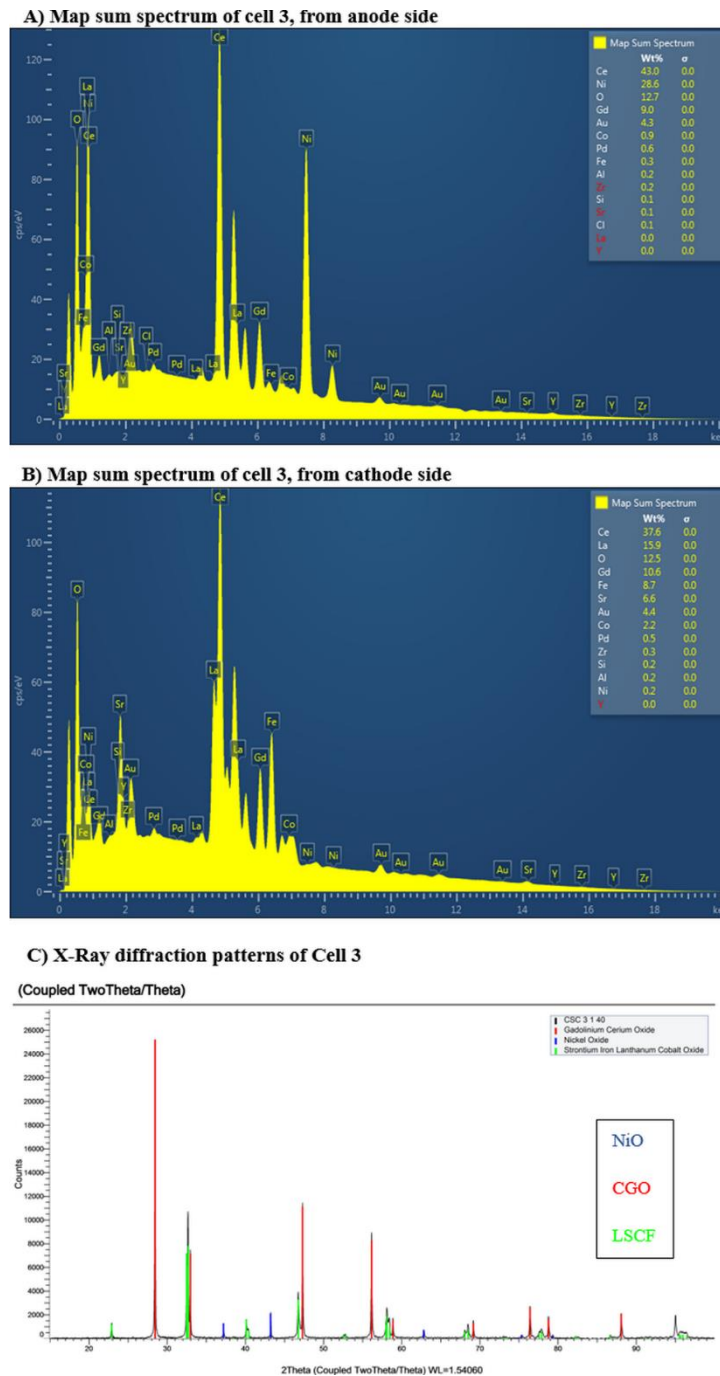


**Figure 6.** Map sum spectrum of cell 3 taken from A) anode side, B) cathode side and C) X-Ray diffraction patterns of Cell 3, the cell possesses a thickness of 60-20-800  $\mu\text{m}$  A-E-C sintered with three 75x75 mm alumina porous cover plate

### 3.2. Cell Performance

Cathode-supported cells were tested in order to examine the functionality of sintered samples as working electrochemical cells, and to investigate the influence of electrolyte and cathode thickness on the cell performance. During performance testing of cells, 100 mL min<sup>-1</sup> nitrogen gas was used as diluting agent at different fuel/oxygen gas (O<sub>2</sub>) mixture (R) so as to reduce the danger of explosion, improve the diffusion and flow of the fuel and oxygen gases as well as for the reactant adsorption and product desorption processes on the anode and cathode [21]. The gas mixture was sent as a flow through (gas flow perpendicular to cathode layer). Figure 7 shows the open circuit voltages and polarization results of cell 1, cell 2 and cell 3, respectively, at different flow rates and gas mixture ratios. Additionally, Table 2 depicts the maximum OCV and power density measurements of these cells.

According to Figure 7A, the OCV of cell 1 diminishes with the increased amount of oxygen gas at both fixed amounts of 50 mL min<sup>-1</sup> methane (CH<sub>4</sub>) and 40 mL min<sup>-1</sup> CH<sub>4</sub>. Maximum OCV and power density of cell 1 were found to be 0.56 V and 25 mW cm<sup>-2</sup>, respectively, in a quite fuel rich gas mixture (gas mixture 4). This can be explained as follows: a fuel rich condition is required to supply more methane to anode surface because of lack of fuel reforming on anode side due to the thin anode thickness in a cathode-supported cell. As a result of increased fuel reforming, more syngas such as hydrogen gas (H<sub>2</sub>) and carbon monoxide (CO) were generated. These products react with oxygen ions (O<sup>2-</sup>) migrating from the cathode side. Therefore, partial pressure differences between two layers increases and thus led to improved OCV and power density. Conversely, the formation of volatile nickel hydroxide Ni(OH)<sub>2</sub> due to presence of water vapor (H<sub>2</sub>O) leads to nickel loss and it becomes severe in oxygen-rich mixture where a higher quantity of water vapor was produced [1], [7]. This could be among the reasons why cells' OCV and power density reduced with increased amount of oxygen gas (see Table 2). However, having high power density at fuel rich condition brings certain problems. For instance, coking of nickel catalyst interfaces, and chemical reactions between methane and oxygen gas or ion could occur on cathode side, and thereby resulting in cell degradation and low cell performance.

The OCV and power density of cell 1 at gas mixture 4 (R: 2.4) and gas mixture 5 (R: 1.6) is higher than that at the gas mixture 1 (R: 2.4) and gas mixture 2 (R: 1.6), respectively whereas the OCV and power density of cell 1 at gas mixture 3 (R: 1) is greater than that of at gas mixture 6 (R: 1). Therefore, the OCVs

and power densities of cell 1 at fixed methane of 40 mL min<sup>-1</sup> is generally higher than that of fixed methane of 50 mL min<sup>-1</sup> at the same fuel /oxygen ratio. In general, increasing gas mixture flow rate has positive effects on cell performance owing to the improved gas exchange at both electrodes which results in reduction in overpotential relating to gas diffusion at both electrodes [1], [3], [21], [22]. However, for cell 1, reduction in the amount of gas mixture by decreasing the fixed amount of CH<sub>4</sub> from 50 mL min<sup>-1</sup> to 40 mL min<sup>-1</sup> (resulting in reduced total flow rate) for the same fuel/oxygen ratio improved cell's OCV as well as its power density (see Figure 7A and Table 2). This could be attributed to the increased residence time of reactant gases on anode electrode where the reforming was limited due to the insufficient anode thickness [22].

Furthermore, for the same anode and cathode thickness (cell 1 and cell 2), decreasing electrolyte thickness from 40 μm to 20 μm had severe effect on power density especially at rich fuel/oxygen condition. Moreover, there is a little reduction in OCV at gas mixture 1 and gas mixture 5 with comparison to cell 1 (see Figure 7 and Table 2). However, at gas mixture 3 and gas mixture 6, the OCV of cell 2 is more than two folds higher than that of cell 1. Therefore, one can generally define that there is an OCV reduction at fuel rich gas mixture (R: 2.4 and R: 1.6) while an increase in OCV is observed at fuel lean condition when cell electrolyte thickness was reduced. In OCV conditions, the oxygen partial pressure differential between the anode-electrolyte and cathode-electrolyte boundaries is the dominant factor that develops the thermodynamic voltage. The reduction in electrolyte thickness allows a faster oxygen gas flux through to the cathode, and the lean condition provides more oxygen overall. Thus, after the partial oxidation on the anode, there is greater net flux of oxygen to the cathode side, resulting in the higher OCV. The OCV reduction could also be attributed to reduced electrolyte thickness leading to better ionic conductivity, thus enabling faster oxygen ion travel from cathode to the anode side. Consequently, oxygen reduction reaction proceeds at the fastest rate for the present condition and therefore depletes oxygen gas at the cathode membrane. The OCV decrease could also be as a result of gas cross-over. Because cells possessing porous electrolytes usually have gas cross-over problem. From the flow-through configuration, the anode reforming and fuel utilization plays a large role. Unused reformat gases generated from anode side such as H<sub>2</sub> and CO can diffuse to the cathode side via porous electrolyte and react parasitically with oxygen gases and thereby causing simply chemical reaction which is not beneficial for SOFC [1], [22], [23]. For the cell

possessing thinner electrolyte, the gas cross over becomes more severe due to easy diffusion of these syngas. Cell 2 possess thinner electrolyte in comparison to cell 1, thereby facilitating higher gas cross-over. In both cases, oxygen partial pressure differences between anode and cathode sides reduce, therefore decreasing OCV, and also further impeding the favorable conditions for methane reforming [1], [22]. The reason for the OCV increment with decreased electrolyte thickness at oxygen rich condition (gas mixture 3 and gas mixture 6) could be explained by the fact that the thinner and porous electrolyte could allow faster oxygen and methane gas transport from cathode side to anode side. Because the gas mixture contacts first to the cathode and pass through electrolyte to anode layer. However, the increment in the amounts of methane diffusion to the anode side will be higher than that of oxygen gas because methane possesses higher diffusivity rate than oxygen gas due to its lower molar mass comparing to  $O_2$ . This leads to more methane reforming on the anode side and thus resulting in more oxygen gas consumption. Therefore, the partial pressure of oxygen increases between two electrodes and thus OCV rises.

The gas cross-over problem does not just lead to OCV reduction but also results in lower fuel partial pressure and limits the use of these fuels for electrochemical reaction, in favor of direct chemical oxidation/reforming. This could explain why less power was obtained from cell 2 in comparison to cell 1 despite the likely lower ohmic losses due to reduction in electrolyte thickness. In addition, the general trend was that the maximum OCV and power density was obtained at fuel rich condition, similar to cell 1. The maximum OCV and power density of cell 2 was found to be 0.38 V and 3.32 mW cm<sup>-2</sup>, respectively at gas mixture 2 (see Figure 7 and Table 2) (around 87% reduction in power density compared to cell 1). According to Figure 7 and Table 2, the OCV of cell 2 generally mitigates with the increased amount of oxygen gas at both fixed amount of 50 mL min<sup>-1</sup> CH<sub>4</sub> and 40 mL min<sup>-1</sup> CH<sub>4</sub> as cell 1. Furthermore, in both cells, the lowest OCV and power density were obtained at lean condition, R=1, and the OCVs were not stable. The oscillation of OCVs might be as a consequence of oxidation-reduction cycle of Ni-cermet anode and accompanying temperature fluctuation at rich oxygen condition [1]. Alternately, the equilibrium may be

dynamically shifting between the favorability towards steam methane reforming, partial methane oxidation and the water-gas shift reactions at the anode side.

Moreover, for the same anode and electrolyte thickness (cell 2 and cell 3), increasing cathode thickness from 400 μm to 800 μm led to considerable OCV and power density reductions at all gas mixtures. Additionally, there were almost no OCV and power density at the oxygen rich gas mixtures (gas mixture 3 and gas mixture 6, see Table 2 and Figure 7). The maximum power and OCV was found to be 1.71 mW cm<sup>-2</sup> and 0.2 V, respectively, at gas mixture 2 (around 51% power density reductions comparing to cell 2). Figure 7C also shows that the OCV and power density of cell 3 generally diminished with the increased amount of oxygen gas at both fixed amount of 50 mL min<sup>-1</sup> CH<sub>4</sub> and 40 mL min<sup>-1</sup> CH<sub>4</sub> as cell 1 and cell 2. The low OCV and power density of the cell 3 might be ascribed to the thicker cathode. Because thick cathode causes high concentration polarization on the cathode side of the cell due to increased difficulties of oxygen gas movement into the inner part of cathode and distance for oxygen ion diffusion from cathode side to anode side of the cell [24]. However, cathode thickness increment also leads to an increase in triple phase boundary for oxygen gas reduction and thus alternately could result in better cell performance. However, the results demonstrated that the benefit of increased triple phase boundary is much less than the negative effect of cathode concentration polarization (mass transport limitation). Furthermore, the LSCF cathode material can also oxidize methane (parasitic catalytic combustion) [1], [25], [26]. Therefore, the increased cathode thickness could lead to more methane oxidation which consume oxygen gas on the cathode side and thereby resulting in low OCV due to decreased oxygen partial pressure difference between cathode and anode. In addition, the reaction product (CO and H<sub>2</sub>) after methane reforming on cathode side can be adsorbed on the cathode surface and leads to a reduction in active area for oxygen gas adsorption [22].

To sum up, the reduced electrolyte thickness and increased cathode thickness selected for the benefit of obtaining planar cathode-supported cell via single step co-sintering unfortunately resulted in severe performance degradation.

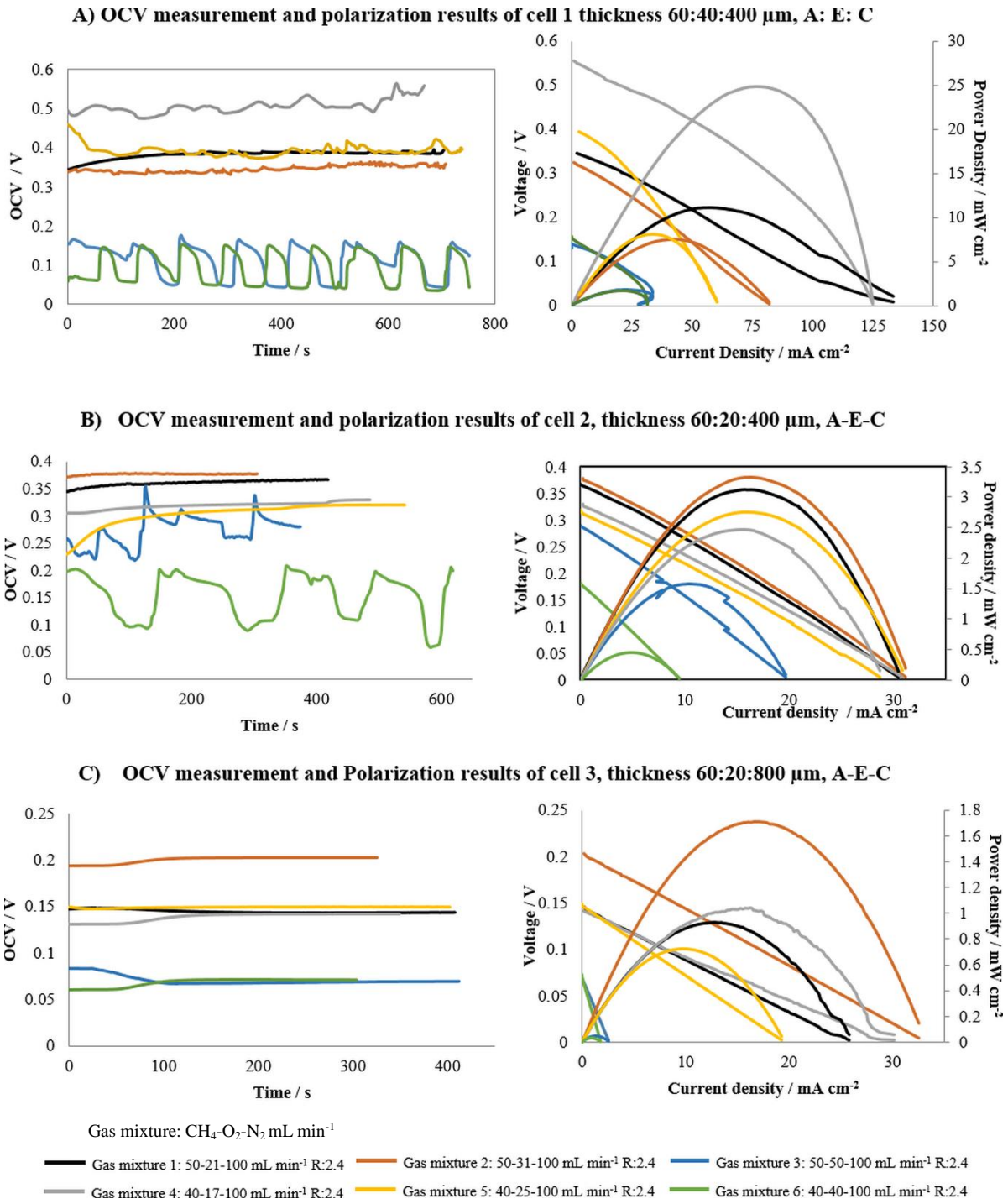


**Figure 7.** OCV Measurement and polarization results of A) Cell 1 thickness 60-40-400  $\mu\text{m}$  A- E-C, B) Cell 2 thickness 60-20-400  $\mu\text{m}$  A-E-C and C) Cell 3 thickness 60-20-800  $\mu\text{m}$  A-E-C, at different flow rate and gas mixture, R, fuel to oxygen ratio.

**Table 2.** The maximum OCV and power density results of cell 1, cell 2 and cell 3 at different gas mixtures.

		Cell 1		Cell 2		Cell 3	
		<i>thickness 60-40-400 <math>\mu\text{m}</math></i>		<i>thickness 60-20-400 <math>\mu\text{m}</math></i>		<i>thickness 60-20-800 <math>\mu\text{m}</math></i>	
		<i>A-E-C</i>		<i>A-E-C</i>		<i>A-E-C</i>	
		OCV / V	Power density / $\text{mW cm}^{-2}$	OCV / V	Power density / $\text{mW cm}^{-2}$	OCV / V	Power density / $\text{mW cm}^{-2}$
Fixed $\text{CH}_4$ / 50 $\text{mL min}^{-1}$  And Fixed $\text{N}_2$ / 100 $\text{mL min}^{-1}$	gas mixture 1 (R:2.4)	0.4	11.1	0.37	3.11	0.143	0.93
	gas mixture 2 (R:1.6)	0.36	7.5	0.38	3.32	0.20	1.71
	gas mixture 3 (R:1)	0.124	1.85	0.28	1.58	0.07	0.05
Fixed $\text{CH}_4$ / 40 $\text{mL min}^{-1}$  And Fixed $\text{N}_2$ / 100 $\text{mL min}^{-1}$	gas mixture 4 (R:2.4)	0.56	24.79	0.33	2.75	0.141	1.04
	gas mixture 5 (R:1.6)	0.394	8.13	0.32	2.47	0.15	0.72
	gas mixture 6 (R:1)	0.05	1.69	0.2	0.45	0.071	0.03

In general, the performance of the cathode-supported SC-SOFCs were found comparatively low with comparison to available results presented in the literature for cathode-supported SC-SOFCs. The cells' performance could be adversely influenced by various reasons. Some were mentioned in the prior section and others could be explained as follows. Lack of fuel utilization due to low selectivity of anode and cathode towards their corresponding gases ( $\text{H}_2$  and  $\text{CO}$  for anode,  $\text{O}_2$  for cathode). It is a general problem for all type of SC SOFCs [1], [22]. This results in quite low cell performance and fuel utilization. Furthermore, the thick and porous electrolyte (thickness varies from 20  $\mu\text{m}$  to 40  $\mu\text{m}$  and porosity around 14%) result in high ohmic losses due to increased ionic transport losses. In addition, CGO electrolyte could be partially reduced at high temperature and low oxygen partial pressure since 600  $^\circ\text{C}$  working temperature is a critical temperature for CGO functionality [12], [27], as predominant on the anode side. This reduction brings about electronic conductivity in a great volume fraction of the electrolyte extending from anode side. Thus electrons flow from anode side to cathode side through electrolyte even at open circuit, and consequently resulting in low power output [1], [12], [28]. Furthermore, the reactivity of oxygen gas for a direct catalytic reaction is higher than the oxygen ion (with the electrochemical charge transfer), thus the oxygen gas easily reacts with  $\text{H}_2$  or  $\text{CO}$  in comparison to  $\text{O}^{2-}$  on the anode side. This can be exacerbated by the

higher thickness of the electrodes. Because the catalytic reactions can occur throughout the electrode thickness, whereas the electrochemical reactions are generally understood to occur within the TPB region, only adjacent to the electrode-electrolyte interfaces.

Another reason for low power output could be the lack of fuel reforming at 600  $^\circ\text{C}$ . Near-complete methane reforming is only achieved at temperatures above 600  $^\circ\text{C}$ . Therefore, for better cell performance, more active fuels such as higher chain hydrocarbons ethane, propane etc. should be used at low temperatures [1].

Moreover, the increased sintering temperature of composite cathode (from 1000  $^\circ\text{C}$  [29] to 1200  $^\circ\text{C}$ ) caused coarse structure of cathode as well as low porosity (see Figure 5). This leads to reduction in the reaction area, and therefore a lack of oxygen reduction reactions [29], [30]. The limitation of oxygen gas transportation through cathode due to low porosity mitigate cell performance owing to increased concentration polarization [31]. Good bonding is also required between particles for better electrical conductivity [29]. However, the CGO conductivities are not as good as it should be on both electrodes (see SEM images of cell 3). This could lead to the oxygen ion interruption through the electrolytes. The weak connections between agglomerated particles escalate the resistance of oxygen ion as well as electrons transfer through the porous cathode [32].

Besides, impurities in electrolyte as well as electrodes have also adverse effect on cell performance. Si can poison the electrolyte material and thus reduce the performance. For instance, silicon can segregate at the grain boundaries of the electrolyte materials, forming insulating siliceous ( $\text{SiO}_2$ ) and thus decreasing conductivity. Si has also detrimental effect on cathode electrode. It can cause serious surface exchange coefficient degradation especially in humidified atmosphere [33]–[35]. For instance, Si can react with Sr in LSCF cathode and cause cathode degradation [36]. The EDS analysis of the cell 3 shows that there was small amount of Si contamination on both electrodes (see Figure 6). Furthermore, strontium carbonate ( $\text{SrCO}_3$ ) is formed on LSCF cathode in atmosphere of  $\text{O}_2$ -carbon dioxide ( $\text{CO}_2$ ) [37], [38]. Thus oxygen activity and surface adsorption on LSCF decreases and it becomes worse with the existence of  $\text{H}_2\text{O}$ . The existence of  $\text{H}_2\text{O}$  with  $\text{CO}_2$  also give rise to strontium oxide ( $\text{SrO}$ ) on LSCF cathode [39]. Zhao et al. [37] defines that the existence of  $\text{H}_2\text{O}$  aggravates the interaction of carbon dioxide with perovskite oxide. Because the  $\text{H}_2\text{O}$ - $\text{CO}_2$  van der Waals complex is formed and later is transformed to bicarbonate at oxygen vacancies and it thereby reduces oxygen reduction reaction.  $\text{CH}_4$  was used for testing of these cathode-supported cells therefore, it is highly possible the formation of  $\text{CO}_2$  and  $\text{H}_2\text{O}$  due to the fuel reforming and electrochemical or chemical reaction of  $\text{H}_2$  or  $\text{CO}$  with oxygen species. Consequently, the formation of  $\text{SrCO}_3$  or  $\text{SrO}$  insulating layers could have caused lower power density. In addition, Ni could be poisoned by the sulfur compounds in the gas mixture (hydrocarbon fuels), even at concentration of 0.1 ppm sulfur compounds [12]. This could also have caused low performance results since the methane used in these experiments has 96% purity. Diffusion of strontium out of LSCF cathode brings about strontium depletion in the cathode and considerably mitigates performance of the cell [24]. The EDS result of cell 3 (see Figure 6) shows that there is not only diffusion of Sr out of LSCF but also Co and Fe, and they were also observed on the anode side. Similarly, Ni was also observed on cathode side. In addition to these impurities, small amount of Al and Zr was also detected on both electrodes. These impurities could also cause less performance by blocking active surface area for either fuel oxidation or oxygen reduction on anode and cathode, respectively. Finally, there was a short circuit observed during experiment of these cells due to silver and gold diffusion from one side to other sides through porous electrolyte. The magnitude of this short circuit was quite high and thereby leading to high power losses. Lastly, Ni oxidation ( $\text{NiO}$  due to

existence of  $\text{O}_2$ ) increases the cell resistance [40] and thus causing low cell performance.

Although SC-SOFCs have low power density with comparison to existing results presented in the literature for cathode-supported planar SC-SOFCs, they can still be considered for Microelectromechanical systems (MEMS) applications, potential sensing functions and power recovery devices from exhaust gases.

#### 4. Conclusions

A cathode-supported planar SOFC for single chamber conditions was made via single step co-sintering fabrication method. Our study showed that determining optimum thickness and thickness ratio of the cell with the optimized hot pressing and sintering conditions leads to better co-sintering results: no crack and delamination but limited curvature at the edge of the cell. Decreasing electrolyte thickness and increasing cathode thickness led to curvature decrease at the edges, but these adjustments were not enough to obtain curvature free cathode-supported cell. Three porous alumina cover plates with a 75x75 mm WxL and mass of 49.35 g was utilized to suppress curvature formation, and as a result, almost a curvature free cathode-supported cell was obtained (cell 3). The fabricated cells' performances were investigated with different gas mixture at 600 °C. The results indicated that increasing cathode thickness and reducing electrolyte thickness had detrimental effects on cell performance despite improved single step co-sinterability of the cell. The maximum power density and OCV of the final planar cell (cell 3, thickness ratio 3-1-40, thickness 60-20-800  $\mu\text{m}$ , A-E-C) were found to be 1.71  $\text{mW cm}^{-2}$  and 0.2 V, respectively, in a gas mixture of 50  $\text{mL min}^{-1}$  of  $\text{CH}_4$ , 31  $\text{mL min}^{-1}$  of  $\text{O}_2$  and 100  $\text{mL min}^{-1}$   $\text{N}_2$ , R:1.6. Furthermore, the maximum power density and OCV among the all cells were measured from the cell 1 (thickness ratio 3-2-20, thickness 60-40-400  $\mu\text{m}$ , A-E-C) as 24.79  $\text{mW cm}^{-2}$  and 0.56 V, respectively, in a fuel rich condition (R:2.4, 40  $\text{mL min}^{-1}$  of  $\text{CH}_4$ , 17  $\text{mL min}^{-1}$  of  $\text{O}_2$  and 100  $\text{mL min}^{-1}$   $\text{N}_2$ ). In general, the performance of the cells was quite low, suggesting that additional work is required to find solutions to the problems mentioned in the previous section. The future study is to test single-step sintered cells under dual chamber conditions in order to investigate their real performance.

## Acknowledgements

The work was supported by the Turkish Ministry of National Education and the EPSRC's the India-UK Collaborative Research Initiative in Fuel Cells project on "Modelling Accelerated Ageing and Degradation of Solid Oxide Fuel Cells" (EP/I037059/1), and also the EPSRC's UK-Korea Collaborative Research Activity in Fuel Cells project on "Novel diagnostic tools and techniques for monitoring and control of SOFC stacks" (EP/M02346X/1). The authors gratefully thank all the supporters mentioned above for their funding.

## Conflict of Interest Statement

There is no conflict of interest between the authors.

## Contributions of the authors

All contributions to this study belong to the authors.

## Statement of Research and Publication Ethics

The study is complied with research and publication ethics

## References

- [1] M. Kuhn and T. W. Napporn, "Single-chamber solid oxide fuel cell technology – from its origins to today's state of the art," *Energies*, vol. 3, no. 1, pp. 57–134, 2010.
- [2] T. Hibino, A. Hashimoto, T. Inoue, J. Tokuno, S. Yoshida, and M. Sano, "Single-chamber solid oxide fuel cells at intermediate temperatures with various hydrocarbon-air mixtures," *Journal of The Electrochemical Society*, vol. 147, no. 8, pp. 2888–2892, 2000.
- [3] M. Yano, A. Tomita, M. Sano, and T. Hibino, "Recent advances in single-chamber solid oxide fuel cells: A review," *Solid State Ionics*, vol. 177, no. 39–40, pp. 3351–3359, 2007.
- [4] T. Suzuki, P. Jasinski, V. Petrovsky, H. U. Anderson, and F. Dogan, "Anode supported single chamber solid oxide fuel cell in CH<sub>4</sub>-air mixture," *Journal of The Electrochemical Society*, vol. 151, no. 9, pp. A1473–A1476, 2004.
- [5] M. Liu and Z. Lü, "Effect of stack configurations on single chamber solid oxide fuel cell, anode-cathode, anode-anode, and cathode-cathode configuration," *Electrochimica Acta*, vol. 104, pp. 64–68, 2013.
- [6] W. Z. Zhu and S. C. Deevi, "A review on the status of anode materials for solid oxide fuel cells," *Materials Science and Engineering A*, vol. 362, no. 1–2, pp. 228–239, 2003.
- [7] A. Faes, A. Hessler-Wyser, A. Zryd, and J. Van Herle, "A review of redox cycling of solid oxide fuel cells anode.," *Membranes*, vol. 2, no. 3, pp. 585–664, 2012.
- [8] K. Huang, A. Zampieri, and M. Ise, "Cathode polarizations of a cathode-supported solid oxide fuel cell," *Journal of The Electrochemical Society*, vol. 157, no. 10, p. B1471, 2010.
- [9] R. K. Bordia and E. A. Olevsky, *Advances in sintering science and technology*. California: John Wiley & Sons, 2009.
- [10] L. C. De Jonghe and M. N. Rahaman, "Sintering of ceramics," in *Handbook of advanced ceramics*, S. Somiya, F. Aldinger, R. M. Spriggs, K. Uchino, K. Koumoto, and M. Kaneno, Eds. San Diego, California: Elsevier, 2003, pp. 187–264.
- [11] M. N. Rahaman, "Sintering and microstructure development," in *Ceramic processing*, Florida: Taylor&Francis Group, 2007, pp. 365–441.
- [12] S. C. Singhal and K. Kendall, *High temperature solid oxide fuel cells: Fundamentals, design and applications*. Oxford: Elsevier Advanced Technology, 2003.
- [13] A. Hagen, R. B. Menon, P. V. Hendriksen, S. Ramousse, and P. H. Larsen, "Properties and performance of SOFCs produced on a pre-pilot plant scale," *Fuel Cells*, vol. 6, no. 2, pp. 146–150, 2006.
- [14] H. Wang, Z. Gao, and S. A. Barnett, "Anode-supported solid oxide fuel cells fabricated by single step reduced-temperature co-firing," *Journal of The Electrochemical Society*, vol. 163, no. 3, pp. F196–

F201, 2016.

- [15] J. H. Myung, H. J. Ko, C. H. Im, J. Moon, and S. H. Hyun, "Development of solid oxide fuel cells (SOFCs) by tape-casting and single-step co-firing of monolithic laminates," *International Journal of Hydrogen Energy*, vol. 39, no. 5, pp. 2313–2319, 2014.
- [16] G. Ye, F. Ju, C. Lin, S. Gopalan, and U. Pal, "Single-step co-firing technique for SOFC fabrication," in *Advances in Solid Oxide Fuel Cells*, N. P. Bansal, D. Zhu, and W. M. Kriven, Eds. Florida: The American ceramic Society, 2005, pp. 25–32.
- [17] "Maryland Tape Casting." [Online]. Available: <http://www.marylandtapecasting.com/>.
- [18] Y. Sayan, V. Venkatesan, E. Guk, H. Wu, and J. S. Kim, "Single-step fabrication of an anode supported planar single-chamber solid oxide fuel cell," *International Journal of Applied Ceramic Technology*, vol. 15, no. 6, pp. 1375–1387, 2018.
- [19] Y.-G. Choi *et al.*, "Ceria-based electrolyte reinforced by sol–gel technique for intermediate-temperature solid oxide fuel cells," *International Journal of Hydrogen Energy*, vol. 38, no. 23, pp. 9867–9872, 2013.
- [20] C. Montgkolkachit and S. Wanakitti, "Characterization of (La,Sr)(Co,Fe)O<sub>3-δ</sub> ferrite-based cathodes for intermediate-temperature SOFCs," *Journal of Metals, Materials and Minerals*, vol. 18, no. 2, pp. 33–36, 2008.
- [21] Y. Tian *et al.*, "Effect of gas supply method on the performance of the single-chamber SOFC micro-stack and the single cells," *Journal of Solid State Electrochemistry*, vol. 17, no. 1, pp. 269–275, 2013.
- [22] I. Riess, "On the single chamber solid oxide fuel cells," *Journal of Power Sources*, vol. 175, no. 1, pp. 325–337, 2008.
- [23] P. Briault, M. Rieu, R. Laucournet, B. Morel, and J.-P. Viricelle, "Anode supported single chamber solid oxide fuel cells operating in exhaust gases of thermal engine," *Journal of Power Sources*, vol. 268, pp. 356–364, 2014.
- [24] C. Sun, R. Hui, and J. Roller, "Cathode materials for solid oxide fuel cells: a review," *Journal of Solid State Electrochemistry*, vol. 14, no. 7, pp. 1125–1144, 2009.
- [25] J. C. F. II and S. S. C. Chuang, "Investigating the CH<sub>4</sub> reaction pathway on a novel LSCF anode catalyst in the SOFC," *Catalysis Communications*, vol. 10, no. 6, pp. 772–776, 2009.
- [26] Y. Hao, Z. Shao, J. Mederos, W. Lai, D. G. Goodwin, and S. M. Haile, "Recent advances in single-chamber fuel-cells: Experiment and modeling," *Solid State Ionics*, vol. 177, no. 19–25, pp. 2013–2021, 2006.
- [27] J. Viricelle, S. Udroui, G. Gadacz, M. Pijolat, and C. Pijolat, "Development of single chamber solid oxide fuel cells ( SCFC )," no. 4, pp. 683–692, 2010.
- [28] R. M. Ormerod, "Solid oxide fuel cells," *Chemical Society Reviews*, vol. 32, no. 1, pp. 17–28, 2003.
- [29] Y. Leng, S. H. Chan, and Q. Liu, "Development of LSCF-GDC composite cathodes for low-temperature solid oxide fuel cells with thin film GDC electrolyte," *International Journal of Hydrogen Energy*, vol. 33, no. 14, pp. 3808–3817, 2008.
- [30] C. Zhang, Y. Lin, R. Ran, and Z. Shao, "Improving single-chamber performance of an anode-supported SOFC by impregnating anode with active nickel catalyst," *International Journal of Hydrogen Energy*, vol. 35, no. 15, pp. 8171–8176, 2010.
- [31] M. Liu, M. Liu, D. Ding, K. Blinn, X. Li, and L. Nie, "Enhanced performance of LSCF cathode through surface modification," *International Journal of Hydrogen Energy*, vol. 37, no. 10, pp. 8613–8620, 2012.
- [32] C. Ding *et al.*, "Effect of thickness of Gd<sub>0.1</sub>Ce<sub>0.9</sub>O<sub>1.95</sub> electrolyte films on electrical performance of anode-supported solid oxide fuel cells," *Journal of Power Sources*, vol. 195, no. 17, pp. 5487–5492,

2010.

- [33] E. Bucher and W. Sitte, “Long-term stability of the oxygen exchange properties of  $(\text{La},\text{Sr})_{1-z}(\text{Co},\text{Fe})\text{O}_{3-\delta}$  in dry and wet atmospheres,” *Solid State Ionics*, vol. 192, no. 1, pp. 480–482, 2011.
- [34] E. Bucher, W. Sitte, F. Klauser, and E. Bertel, “Impact of humid atmospheres on oxygen exchange properties, surface-near elemental composition, and surface morphology of  $\text{La}_{0.6}\text{Sr}_{0.4}\text{CoO}_{3-\delta}$ ,” *Solid State Ionics*, vol. 208, pp. 43–51, 2012.
- [35] E. Bucher and W. Sitte, “Defect chemical modeling of  $(\text{La}, \text{Sr})(\text{Co}, \text{Fe})\text{O}_{3-\delta}$ ,” *Journal of Electroceramics*, vol. 13, no. 1–3, pp. 779–784, 2004.
- [36] Z. Yang, M. Guo, N. Wang, C. Ma, J. Wang, and M. Han, “A short review of cathode poisoning and corrosion in solid oxide fuel cell,” *International Journal of Hydrogen Energy*, vol. 42, no. 39, pp. 24948–24959, 2017.
- [37] Z. Zhao *et al.*, “High and low temperature behaviors of  $\text{La}_{0.6}\text{Sr}_{0.4}\text{Co}_{0.2}\text{Fe}_{0.8}\text{O}_{3-\delta}$  cathode operating under  $\text{CO}_2/\text{H}_2\text{O}$ -containing atmosphere,” *International Journal of Hydrogen Energy*, vol. 38, no. 35, pp. 15361–15370, 2013.
- [38] J. Hayd, L. Dieterle, U. Guntow, D. Gerthsen, and E. Ivers-Tiffée, “Nanoscaled  $\text{La}_{0.6}\text{Sr}_{0.4}\text{CoO}_{3-\delta}$  as intermediate temperature solid oxide fuel cell cathode: Microstructure and electrochemical performance,” *Journal of Power Sources*, vol. 196, no. 17, pp. 7263–7270, 2011.
- [39] R. R. Liu *et al.*, “Influence of water vapor on long-term performance and accelerated degradation of solid oxide fuel cell cathodes,” *Journal of Power Sources*, vol. 196, no. 17, pp. 7090–7096, 2011.
- [40] Z. H. Wang *et al.*, “Redox tolerance of thin and thick Ni/YSZ anodes of electrolyte-supported single-chamber solid oxide fuel cells under methane oxidation conditions,” *Fuel Cells*, vol. 13, no. 6, pp. 1109–1115, 2013.